Iranian Journal of Astronomy and Astrophysics
Vol. 8, No. 2, Autumn 2021
©Available online at http://journals.du.ac.ir
DOI:10.22128/IJAA.2021.495.1106

Iranian Journal of Astronomy and Astrophysics

Brueckner Events Oscillations in Solar Transition Region

Sima Zeighami*[1] · Ehsan Tavabi[2]
[1] Department of Physics, Tabriz Branch, Islamic Azad University, Tabriz, Iran;
*email: zeighami@iaut.ac.ir
[2] Physics Department, Payame Noor University (PNU), 19395-3697-Tehran, I. R. of Iran;
email: e_tavabi@pnu.ac.ir

Abstract. We study Brueckner event Oscillations in Solar Transition Region (TR), with simultaneous observations from the Si IV 1402Å spectra and slit-jaw images (SJI) 1400 Å based on the *Interface Region Imaging Spectrograph* (*IRIS*), on August 17 and January 27, 2014. Studying of these events can significantly help us understand the mechanisms of the mass and energy transporting from chromosphere toward TR and corona. We obtained intensity profiles from spectrum perpendicular to the slit in three altitudes from the limb, and then by fitting Gaussian intensity profiles, the transverse fluctuations up to 3200 km altitude along the slit were computed. We observed that Si IV spectra shows blue and red wing enhancements in the line profiles indicating upward and downward twisted. Average of Doppler velocities in the first and second data for the three altitudes were obtained 35 and 80 $km\ s^{-1}$ respectively. The results of wavelet analysis of fluctuations revealed dominant periods of 1.5, 3, and 5 minutes. Since the spicules are located almost along the slit of the *IRIS* telescope, it can be concluded that the fluctuations along the line of sight are evidence for kink and twisted Alfvenic supper and hyper sonic waves propagations.

Keywords: TR, Brueckner Events, Coronal Heating, Twisted, Wavelet

1 Introduction

The energy source required to heat the solar TR and corona plasma to a temperature of more than one million Kelvin in the solar dynamic photosphere is a subject of debate in solar physics. The transmission of energy through waves and oscillations can play a significant role to understand the solar dynamical structures and the cause of the sudden rise in temperature of the solar atmosphere to several million Kelvin. propagation of magneto-hydro-dynamic waves is one of the energy transfer mechanisms [24]. These waves in photospheric magnetic tubes can be generated by granular shock wave motions and then propagate along the chromospheric flux tubes and penetrate the corona to transfer energy as heat. Brueckner events are dynamic events that first were observed from the TR with the high-Resolution Telescope and Spectrograph (HRTS) [2]. These events could generate non-Gaussian profiles with strong enhancement of 1-2 arcsec, and typical lifetime of roughly 60 s [4]. At the begining it was believed that such spectra are emitted from turbulent events [2], and for this reason, they are called Brueckner events [12]. After that the term TR Brueckner Events is used [12]. Solar chromosphere is composed of structures called spicules. Typical spicules have about 200 km wide and up to 10,000 km altitude. Jets are narrow gas eruptions about 150 to 250 km in diameter launched from the top of an almost homogeneous layer that stretches for about 3,000 km. Needle-shaped spicules accumulate in areas of the solar supergranular network. Spicules are plasma explosions that occur almost every 5 minutes, and the material inside them moves upwards at a speed of about 80 $km\ s^{-1}$. Spicules are seen even in the quiet Sun. Spicules are ubiquitous, high-velocity jets found in the spectral lines of the dark chromospheric edge. Jets play a powerful role in the mass balance of the solar corona. The brightness of the small jets changes with temperature and altitude, and spectroscopic studies provide valuable information about them through changes in the profile of the spectral lines. Doppler shift in these lines determines the velocity in the line-of-sight and its changes with time and altitude from the surface of the Sun [26]. By shifting the spectral lines, measuring non-thermal rotational velocities is possible that lead to indirect observations of the torsional Alfven waves. These waves can heat the corona by erupting hot plasma and transferring energy as magneto-hydrodynamic waves [36]. So far, two types of spicules have been identified. The type I spicules have a typical lifetime of 3-10 minutes with upward and downward movements on the parabolic paths with a maximum upward speed of 15-40 $km\ s^{-1}$, and the type II have only upward motions with a lifetime up to 50 -150 seconds, and a speed of 30-110 $km\ s^{-1}$ [7]. Type II spicules mainly present in both of the quiet Sun and coronal holes, but in active regions, type I is predominant. A recent study of observations from the *Hinode* and *IRIS* satellites showed that Type II spicules are heated up to the TR temperature [23]. The disk counterparts of type II spicules have been identified through the asymmetry of short-lived chromopheric spectral lines and are inferred as the rotation of the blue or red shifts [1,2,18,25]. The solar magnetical plasma is an elastic and compressible environment that supports the propagation of various types of waves, which is described using magneto-hydro-dynamics (MHD). These waves can disturb parameters such as density, temperature, velocity and magnetic field. There are three types of MHD waves: the first is the incompressible Alfven wave and the second and third are the fast and slow magneto-acoustic waves, which are necessarily compressible. The properties of MHD waves are strongly depend on the angle between the wave vector and the magnetic field, and as a result, these waves affect the structure of the plasma, leading to coupling and dynamic structures of the MHD wave, such as the phase composition, resonant absorption and waveguide propagation which eventually causes the appearance of waves in observational evidence. Waves can also be classified into two dominant modes: sausage and kink. In sausage modes, axial modes $m = 0$ are modes in which the sides of the magnetic tube oscillate in opposite phases and the axis of the tube remains constant. In kink modes with axial mode $m = 1$ are modes in which the sides of the magnetic tube oscillate in phase and the axis of the tube has periodic motion [19]. In a cylindrical model, Alfven waves are rotating waves which can rotate a magnetic tube. Assuming that the spicules are stable waveguides consisting of concentric lines of magnetic fields known as magnetic flux tubes, in an environment with such a magnetic structure, the ground equilibrium state can be considered as a long and narrow tube. In straight cylinders, these modes are incompressible, but in partially rotating cylinders they can be accompanied by plasma density disturbances. The rotating waves disrupt the magnetic field, which in turn causes plasma velocity disturbances in the direction perpendicular to the magnetic field. These waves travel long distances and transmit energy and momentum. Basically, image processing and spectral methods are used to analyze the motion of structures such as spicules and solar jets. In the image processing method, displacements and intensity changes in images are measured [27,28]. In the second method, periodic designs in Doppler shifts are examined by spectrometers [30,37]. Here, we use spectral data from the *IRIS* space telescope. *IRIS* provides a tool for analyzing the thermal structure of the solar atmosphere in the UV wavelength with high spatial and temporal resolution [11]. We analyse intensity of the spectral data by fitting and finding the maximum position of the line spectra. Then we apply the wavelet analysis to determine period of the oscillations in explosive events such as Brueckner events.

2 Observations

We use The observational data from *IRIS*. The *IRIS* spacecraft contained a combination of telescope and spectrograph [11]. *IRIS* obtains observations of the solar TR with high spatial and spectral resolution to investigate the physical processes of fine structures. We used two data set. The first data is taken on 2014 August 17 from 10:06:13 UT to 13:59:48UT, the number of spectral images is 800 frames, the field of view is 175 arcsec $\times$ 167 arcsec. The center of the slit is located at the point X = 827 arcsec and Y = -465 arcsec in the solar coordinates. The second data set is taken on 2014 January 27, from 11:59:55 UT to 12:53:08 UT, The number of spectral images is 324 frames.

The time interval between two consecutive spectral images is 10 seconds. The field of view of this data set is 119arcsec $\times$ 119arcsec. This data network and the center of the slit is located at the point X = 738 arcsec and Y = 629 arcsec in the solar coordinate. The slit in the both of two data is of the fixed slit. Table 1.shows properties of the two dataset. Left panels in Figures 1 and 2 show the solar disk image taken from the *SDO*/AIA (Solar Dynamic Observatory/Atmospheric Imaging Assembly), recorded on August 17, 2014 at 10:56:07. The black box on the image shows the field of view in *IRIS*. Middle panels of Figures 1 and 2 are unsharp masked SJI 1400 Å images taken at 10:56:07 UT on August 17 and January 27, 2014, respectively. The vertical white line in the middle marks the location of the slit. Right panels in Figures 1 and 2 are SiIV spectral image taken at the same time along the vertical slit. Three purple transverse dashed lines show the altitudes along which Doppler velocity is studied. The distance of successive selected altitudes is 1500 km.

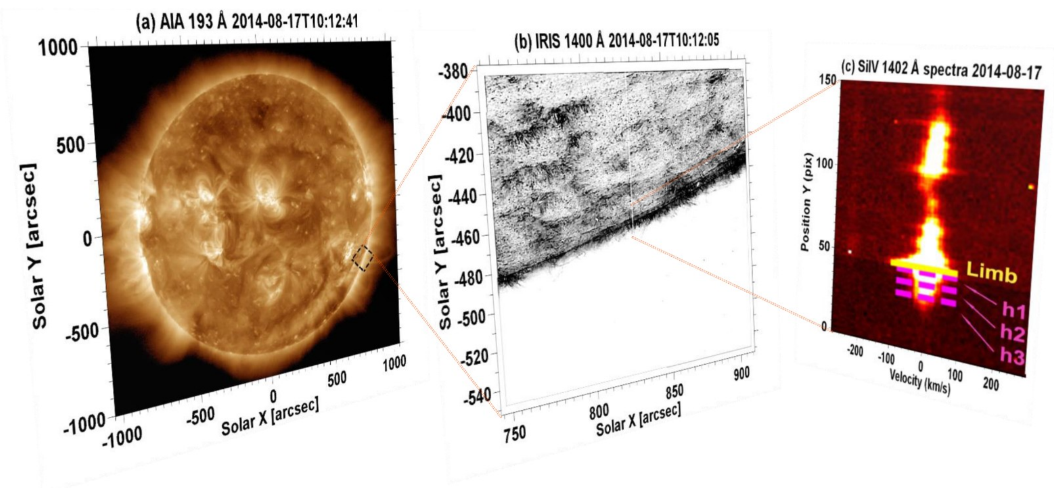

Figure 1: left panel is the solar disk image (193 Å) taken from the SDO / AIA recorded on August 17, 2014 at 10:56:07. The black box shows the field of view in *IRIS*. Middle panel is an unsharp masked SJI 1400 image taken at 10:56:07 UT on 2014 Ague 17. The vertical white line in the middle marks the location of the slit. Right panel is Si IV spectral image taken at the same time along the vertical slit. Three purple horizontal dashed lines show the altitudes along which intensity of spectrum and Doppler shifts is studied. The distance of successive altitudes is 1600 km.

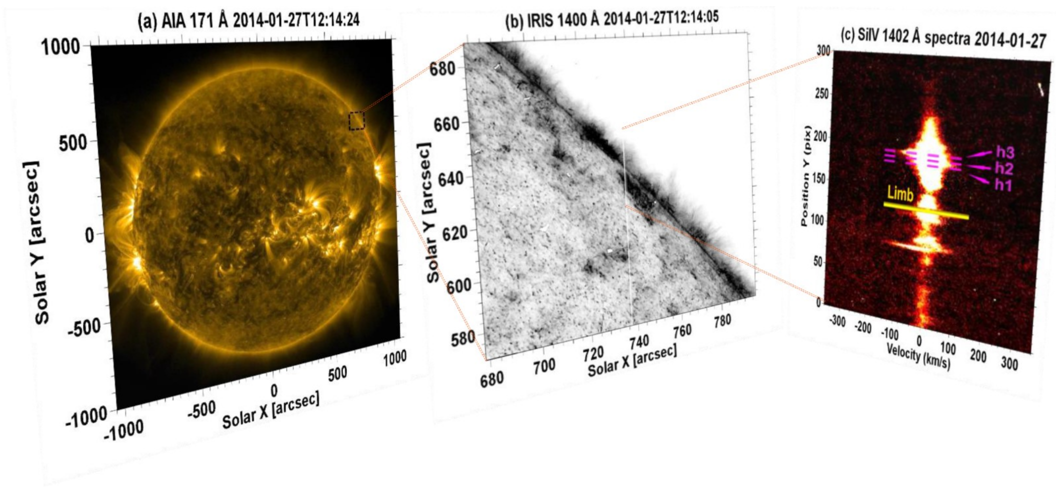

Figure 2: left panel is solar disk image (171 Å) taken from the SDO / AIA , recorded on January 27, 2014 at 12:14:24UT. The black box shows the field of view in *IRIS*. Middle panel is an unsharp masked SJI 1400 image taken at 12:14:05 UT on 2014 January 27. The vertical white line in the middle indicate the location of the slit. Right panel is Si IV spectral image taken at the same time along the vertical slit. Three purple horizontal dashed lines show the altitudes along which intensity of spectrum is studied. The distance of successive altitudes is 1600 km.

Table 1: Properties of the two Datasets.

Date, OBSID	Start and end times (U.T.)	X center Y-center (arcsec)	SJI Cadence (s)	SJI Pixel size (arcsec)	SJI X-FOV Y-FOV (arcsec)	Raster Cadence (s)	Slit length (arcsec)
2014-08-17 380011404	10:06:13 13:59:48	827, -465	32	0.17	167 175	16	175
2014-01-27 3800009253	11:59:55 12:53:08	827, -465	32	0.17	119 119	10	119

3 Data analysis

After preparing the spectral images, it is chosen a time interval in which we see Doppler shifts with significant fluctuations with respect to the central wavelength (red and blue shifts). This range starts from the first frame to the 90^{th} spectral image at the begining of time series, equivalent to approximately 25 minutes, and from 226^{th} to the 326^{th} spectral images for the second time series, almost 19 minutes. Blue and red shifting means moving the structure of the event closer and far from the observer, respectively. To determine the Doppler enhancements in the explosive events and to investigate of maximum position of these displacements, by programming MATLAB and ssw/IDL spectral, intensity profiles was selected from the spectral images along the three altitudes which indicated by h1, h2, and h3 in the left panel of Figures 1 and 2. The time slice diagrams of the profiles can be ready according to the Figures (3a) and (6a) for both data. In these time slices, the horizontal and vertical axis indicate the time and Doppler velocities, respectively. Figures

(3b-3d) demonstrate some examples of the SiIV spectral images in altitude h1 which are overplotted with the line profiles from the pixel that is marked with a red bar on the left. The line profiles plotted as a function of velocity are correspond to the blue shift, without shift, and red shift, respectively. Blue profiles are original profiles and red dashed profiles are their Gaussian fits. Figures (4b-4d) and (5b-5d) are the same (3b-3d) but for altitudes h2 and h3, respectively. Figures (6b-6d), (7b-7d) and (8b-8d) are the same but for the second data.

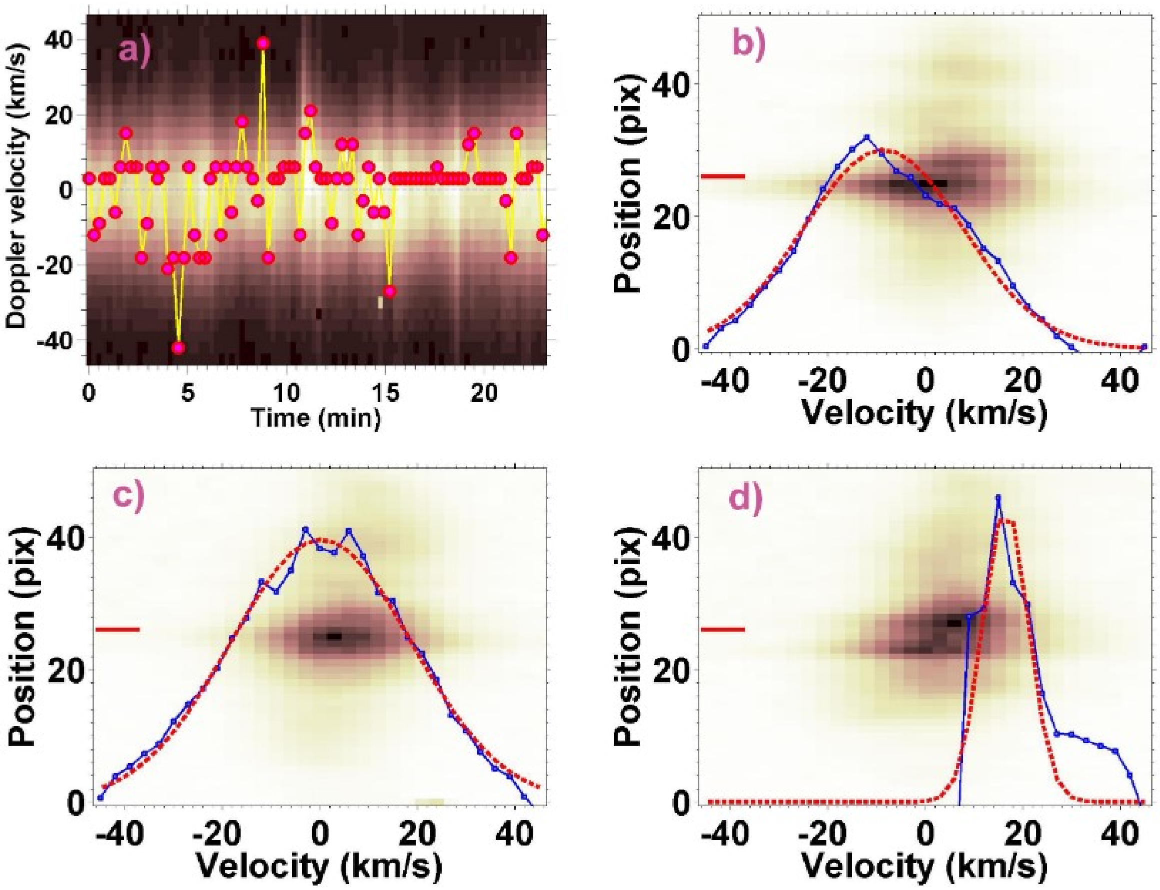

Figure 3: (a) Temporal evolution of Si IV 1402 Å spectra which are overplotted position of maximum intensity by red circles for the first data recorded on January 17, 2014, along the first altitude indicated by (h1) in the left panel of Figure 1. (b)-(d) represent examples of the Si IV spectral images which are overplotted with the line profiles from the pixel that is marked with a red bar on the left. The line profiles in (a)-(d) plotted as a function of velocity are correspond to blue shift, without shift, and red shift, respectively. Blue profiles are original profiles and red dashed profiles are their averaged Gaussian fits.

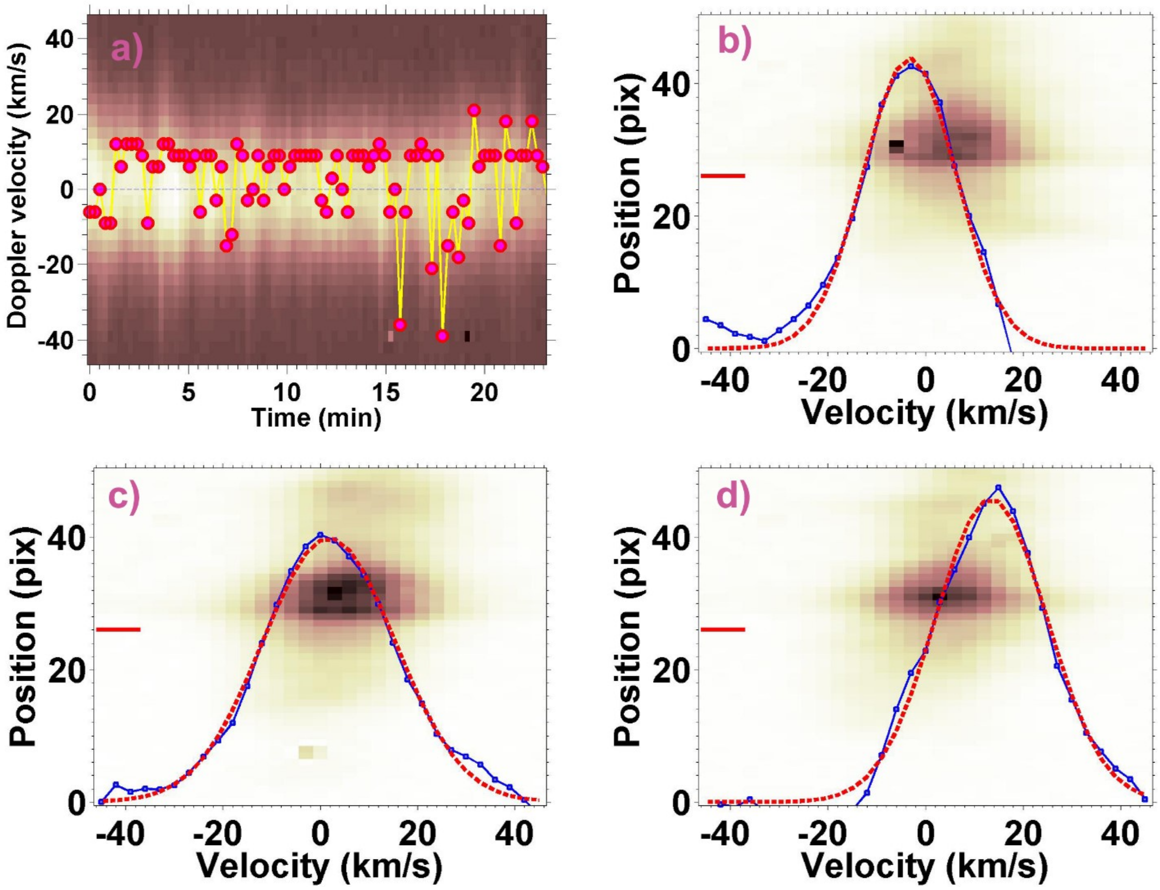

Figure 4: (a) Temporal evolution of Si IV 1402 Å spectra which are overplotted position of maximum intensity by red circles for the first data recorded on August 17, 2014, along the second altitude indicated by (h2) in the left panel of Figure 1. (b)-(d) represent examples of the Si IV spectral images which are overplotted with the line profiles from the pixel that is marked with a red bar on the left. The line profiles in (a)-(d) plotted as a function of velocity are correspond to blue shift, without shift, and red shift, respectively. Blue profiles are original profiles and red dashed profiles are their averaged Gaussian fits.

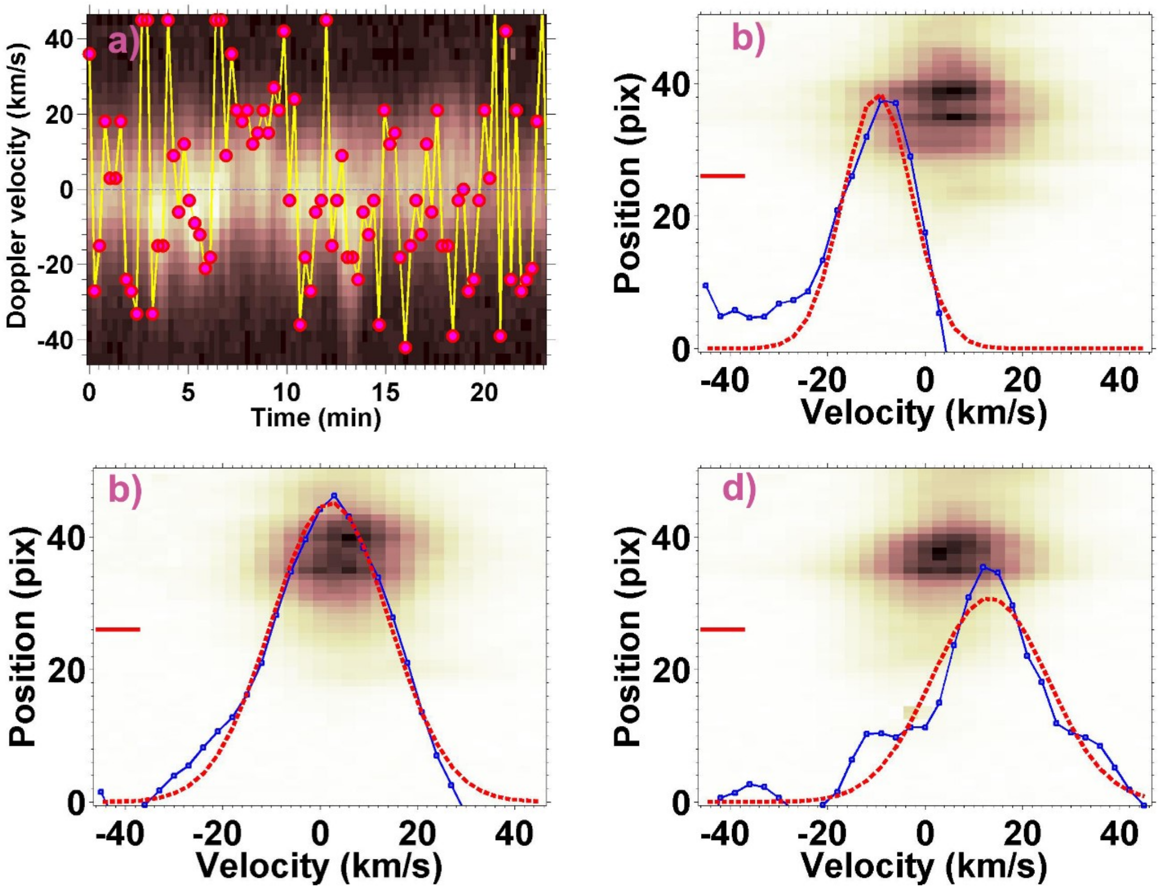

Figure 5: (a) Temporal evolution of Si IV 1402 Å spectra which are overplotted position of maximum intensity by red circles for the first data recorded on August 17, 2014, along the third altitude indicated by (h3) in the left panel of Figure 1. (b)-(d) represent examples of the Si IV spectral images which are overplotted with the line profiles from the pixel that is marked with a red bar on the left. The line profiles in (a)-(d) plotted as a function of velocity are correspond to blue shift, without shift, and red shift, respectively. Blue profiles are original profiles and red dashed profiles are their averaged Gaussian fits.

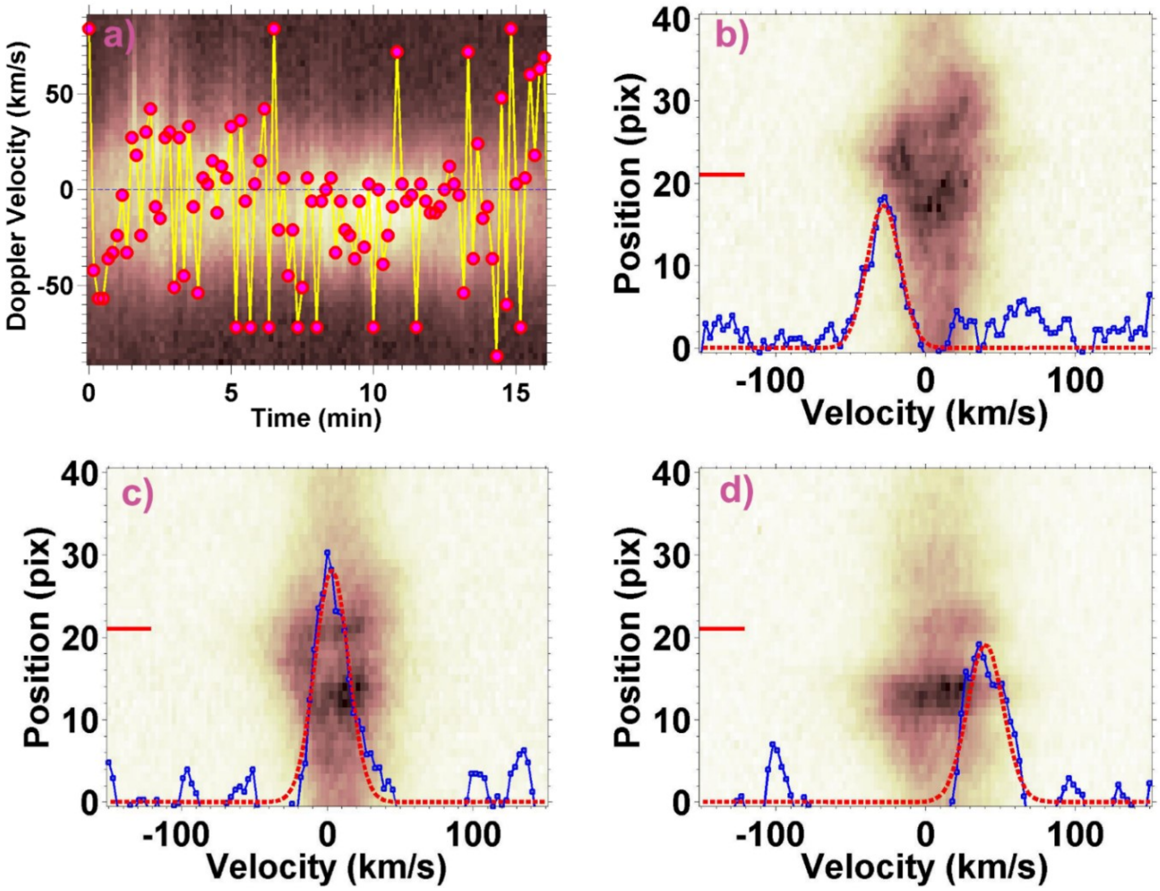

Figure 6: (a) Temporal evolution of Si IV 1402 Å spectra which are overplotted position of maximum intensity by red circles for the second data recorded on January 27, 2014, along the second altitude indicated by (h1) in the left panel of Figure 1. (b)-(d) represent examples of the Si IV spectral images which are overplotted with the line profiles from the pixel that is marked with a red bar on the left. The line profiles in (a)-(d) plotted as a function of velocity are correspond to blue shift, without shift, and red shift, respectively. Blue profiles are original profiles and red dashed profiles are their averaged Gaussian fits.

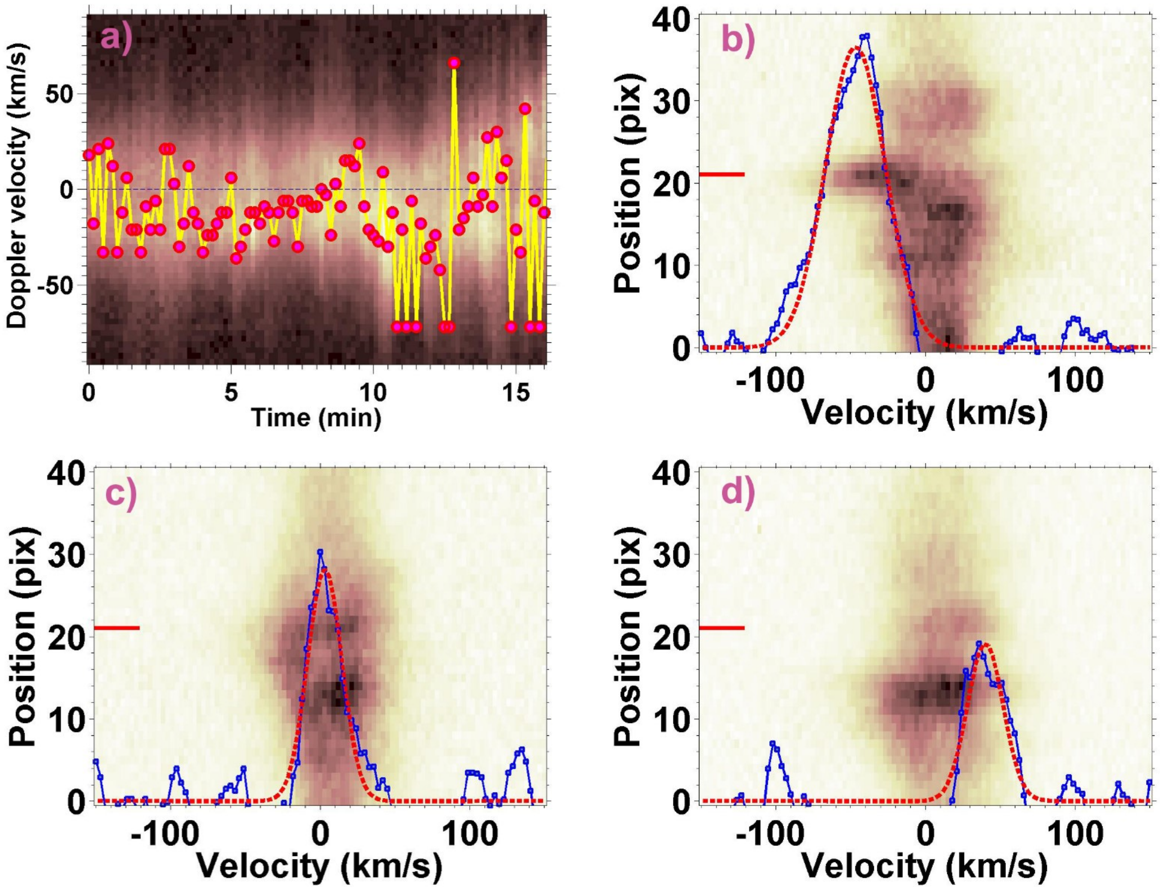

Figure 7: (a) Temporal evolution of Si IV 1402 Å spectra which are overplotted position of maximum intensity by red circles for the second data recorded on January 27, 2014, along the third altitude indicated by (h2) in the left panel of Figure 1. (b)-(d) represent examples of the Si IV spectral images which are overplotted with the line profiles from the pixel that is marked with a red bar on the left. The line profiles in (a)-(d) plotted as a function of velocity are correspond to blue shift, without shift, and red shift, respectively. Blue profiles are original profiles and red dashed profiles are their averaged Gaussian fits.

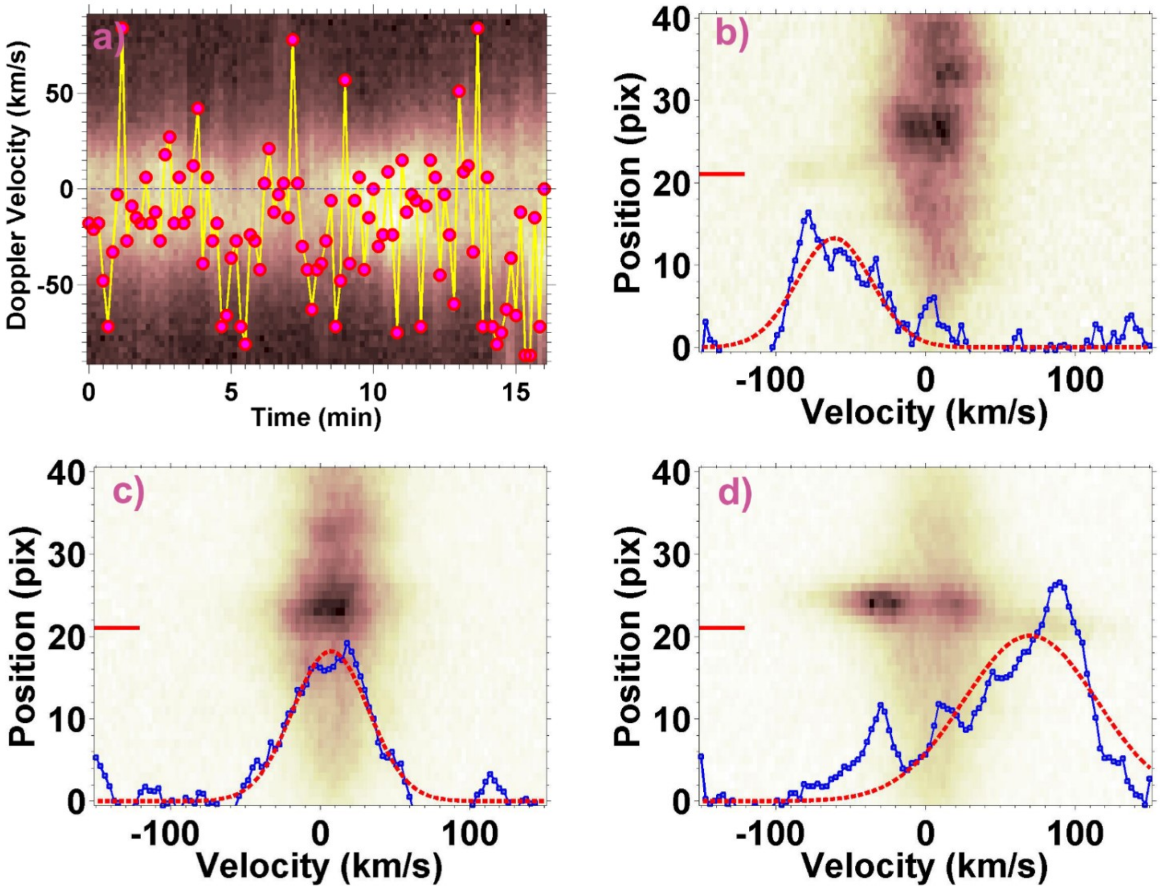

Figure 8: (a) Temporal evolution of Si IV 1402 Å spectra which are overplotted position of maximum intensity by red circles for the second data recorded on January 27, 2014, along the third altitude indicated by (h3) in the left panel of Figure 1. (b)-(d) represent examples of the Si IV spectral images which are overplotted with the line profiles from the pixel that is marked with a red bar on the left. The line profiles in (a)-(d) plotted as a function of velocity are correspond to blue shift, without shift, and red shift, respectively. Blue profiles are original profiles and red dashed profiles are their averaged Gaussian fits.

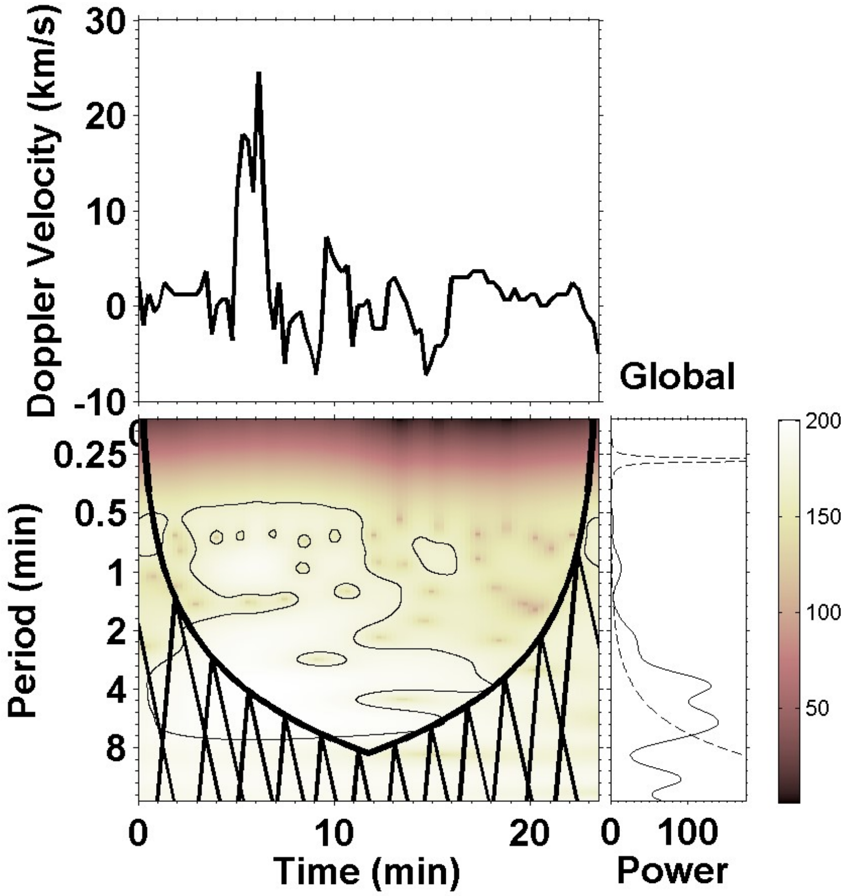

Figure 9: Results of wavelet analysis of spectral fluctuations of Si IV 1402 Å spectra for the first data recorded on August 17, 2014, along the first altitude indicated by (h1) in the left panel of Figure 1. The top panel shows Doppler velocity fluctuations relative to the time and the bottom panel indicate the wavelet analysis of the oscillations over 24 minutes. 4 and 5 minute fluctuations are predominant. The hatched area is the shape of an area in which the wavelet power spectrum is disturbed due to the effect of the endpoints of finite longitudinal signals. The hatched area outside the curve are used to remove the edge effects and indicate the cone of influence region (COI) where the wavelet power spectra are distorted because of the influence of the end points of finite-length signals. These effects will not be reliable and will be eliminated.

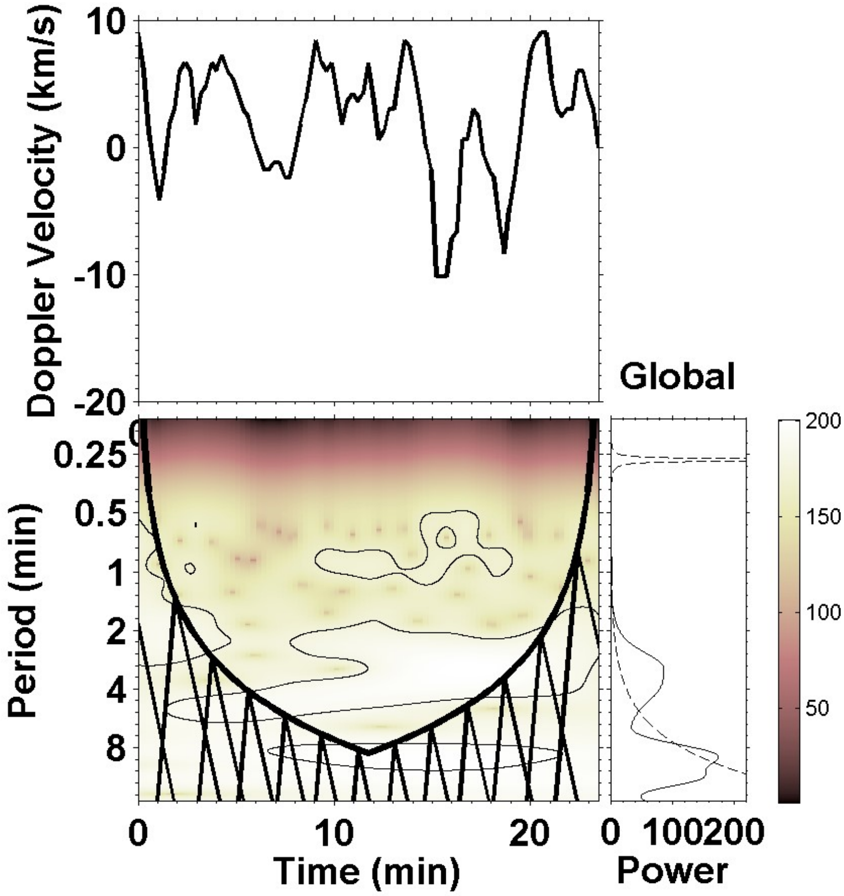

Figure 10: Results of wavelet analysis of spectral fluctuations of Si IV 1402 Å spectra for the first data recorded on August 17, 2014, along the second altitude indicated by (h2) in the left panel of Figure 1. The top panel shows Doppler velocity fluctuations relative to the time and the bottom panel indicate the wavelet analysis of the oscillations over 24 minutes. 3 minute fluctuations are predominant. The hatched area is the shape of an area in which the wavelet power spectrum is disturbed due to the effect of the endpoints of finite longitudinal signals. The hatched area outside the curve are used to remove the edge effects and indicate the cone of influence region (COI) where the wavelet power spectra are distorted because of the influence of the end points of finite-length signals. These effects will not be reliable and will be eliminated.

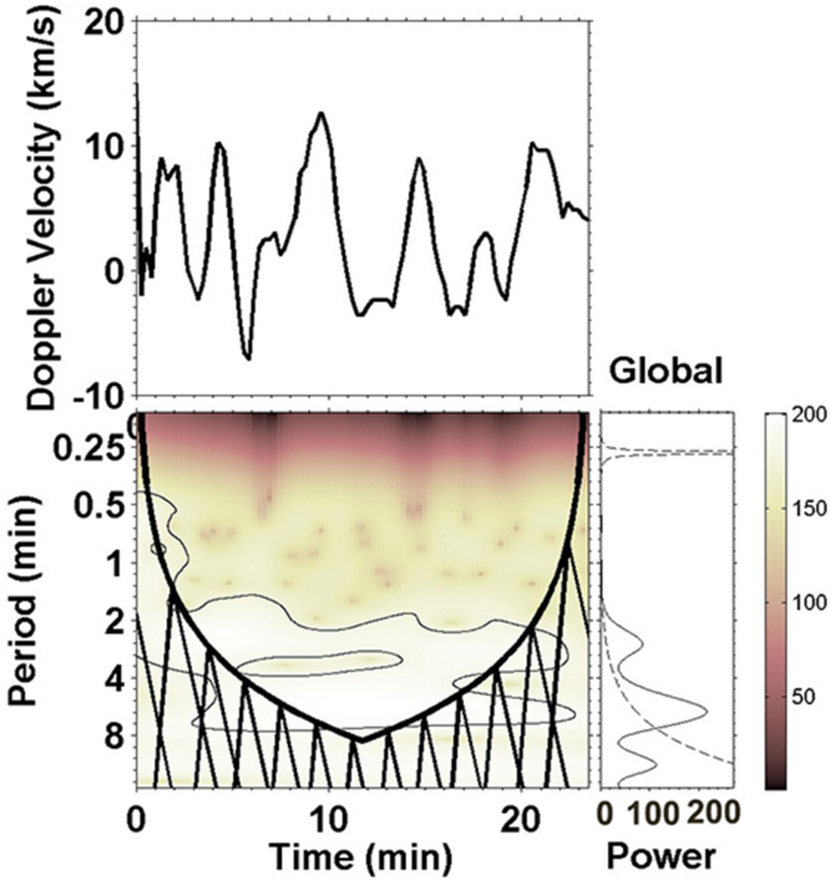

Figure 11: Results of wavelet analysis of spectral fluctuations of Si IV 1402 Å spectra for the first data recorded on August 17, 2014, along the third altitude indicated by (h3) in the left panel of Figure 1. The top panel shows Doppler velocity fluctuations relative to the time and the bottom panel indicate the wavelet analysis of the oscillations over 24 minutes. 3 and 5 minute fluctuations are predominant. The hatched area is the shape of an area in which the wavelet power spectrum is disturbed due to the effect of the endpoints of finite longitudinal signals. The hatched area outside the curve are used to remove the edge effects and indicate the cone of influence region (COI) where the wavelet power spectra are distorted because of the influence of the end points of finite-length signals. These effects will not be reliable and will be eliminated.

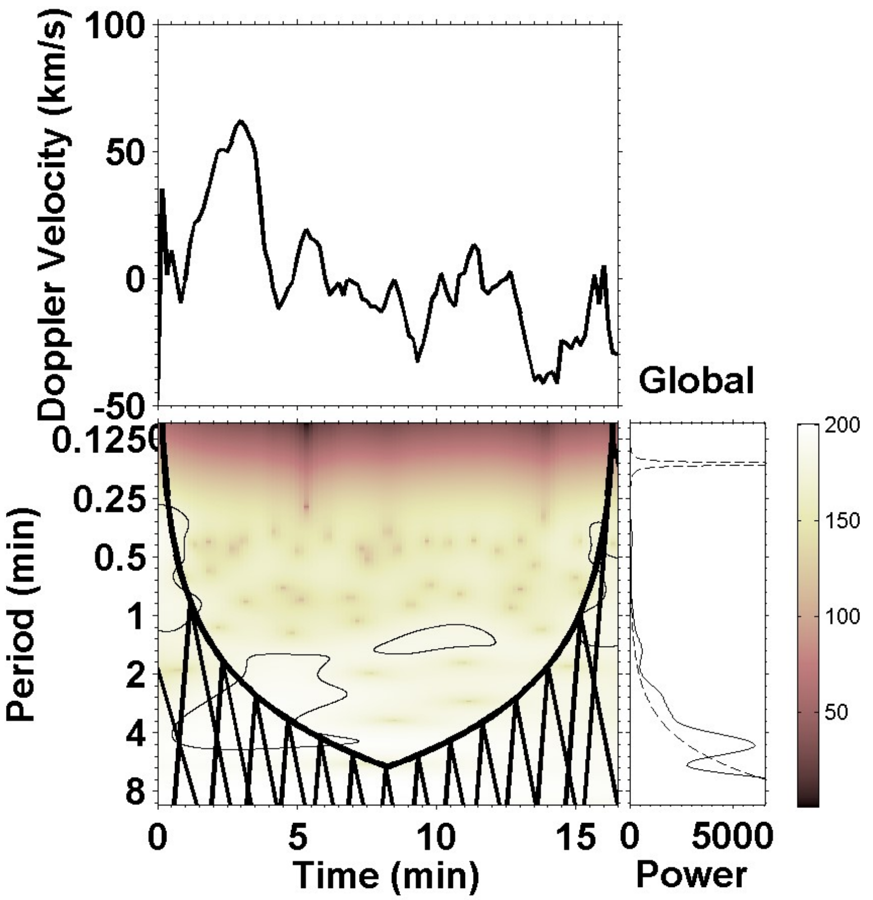

Figure 12: Results of wavelet analysis of spectral fluctuations of Si IV 1402 Å spectra for the second data recorded on January 27, 2014, along the first altitude indicated by (h1) in the left panel of Figure 2 The top panel shows Doppler velocity fluctuations relative to the time and the bottom panel indicate the wavelet analysis of the oscillations over 17 minutes. 5 minute fluctuations are predominant. The hatched area is the shape of an area in which the wavelet power spectrum is disturbed due to the effect of the endpoints of finite longitudinal signals. The hatched area outside the curve are used to remove the edge effects and indicate the cone of influence region (COI) where the wavelet power spectra are distorted because of the influence of the end points of finite-length signals. These effects will not be reliable and will be eliminated.

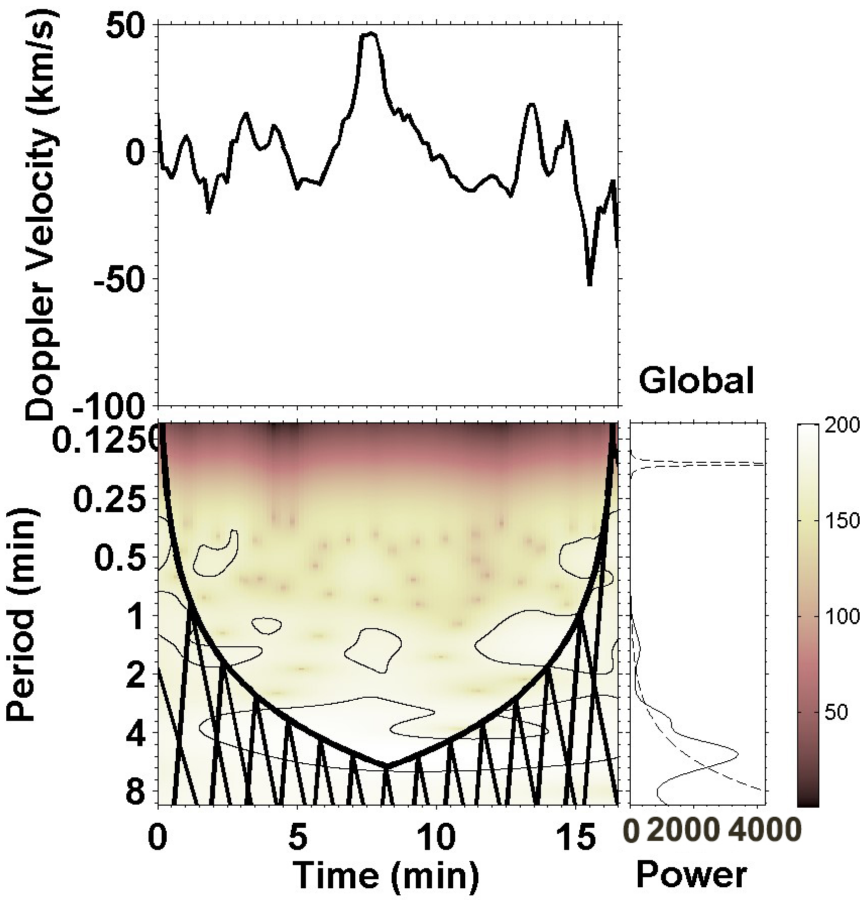

Figure 13: Results of wavelet analysis of spectral fluctuations of Si IV 1402 Å spectra for the second data recorded on January 27, 2014, along the third altitude indicated by (h2) in the left panel of Figure 2. The top panel shows Doppler velocity fluctuations relative to the time and the bottom panel indicate the wavelet analysis of the oscillations over 17 minutes. 1.5 and 3 minute fluctuations are predominant. The hatched area is the shape of an area in which the wavelet power spectrum is disturbed due to the effect of the endpoints of finite longitudinal signals. The hatched area outside the curve are used to remove the edge effects and indicate the cone of influence region (COI) where the wavelet power spectra are distorted because of the influence of the end points of finite-length signals. These effects will not be reliable and will be eliminated.

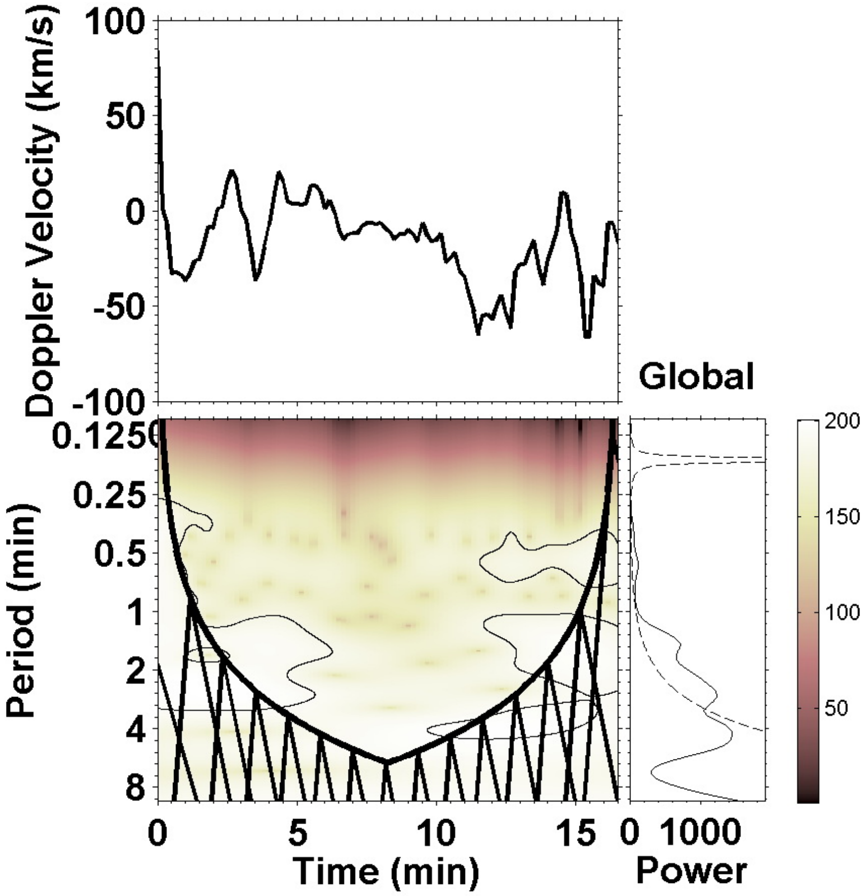

Figure 14: Results of wavelet analysis of spectral fluctuations of Si IV 1402 Å spectra for the first data recorded on August 17, 2014, along the first altitude indicated by (h3) in the left panel of Figure 1. The top panel shows Doppler velocity fluctuations relative to the time and the bottom panel indicate the wavelet analysis of the oscillations over 24 minutes. 4 and 5 minute fluctuations are predominant. The hatched area is the shape of an area in which the wavelet power spectrum is disturbed due to the effect of the endpoints of finite longitudinal signals. The hatched area outside the curve are used to remove the edge effects and indicate the cone of influence region (COI) where the wavelet power spectra are distorted because of the influence of the end points of finite-length signals. These effects will not be reliable and will be eliminated.

By using these information for some time, a while, a set of time signals is obtained. The signals are a set of physical quantities that change according to an independent parameter or variable. If the variable is time, the signal is a temporal signal, and if it is location, it is called a spatial signal. These signals contain information about their sources and by processing the signals, the behavior of the sources can be analyzed. So far, various tools for signal processing have been introduced, of which Fourier analysis is a traditional and long-standing tool. But a an influential tool called wavelet analysis has been around since the early 1980, and in the future, signal processing may play the same role in science and technology as electronics did in the past. The Morlete-based wavelet analysis method is used to study the periodicity of Doppler fluctuations, which is an important tool for oscillation processing [32]. The reason for the conversion is that the information about a signal in one domain (often the time domain) is not very obvious, but in the other domain, i.e. the converted domain (for example, the frequency domain) is more obvious. The basis of the Fourier analysis is sine waves that range from infinitely positive to infinitely negative. This limits the ability to analyze different types of data in different forms, so the properties of these waves are not suitable for analyzing discrete signals in the solar plasma. Wavelet analysis converts signals into both temporal and spatial intervals, which seems very appropriate due to the inherent nature of structures such as solar spicules.

One of the significant properties of wavelet analysis is its desired shape so that a suitable wavelet function (base function) is selected for each type of structure. Wavelet transformations of oscillations at three altitude are seen in Figures (9-11) and (12-14) for both sets. Top panels of Figures (9-14) show Doppler velocity fluctuations relative to the time for Si IV 1402 Å spectra for the two data recorded on August 17, 2014, and January 27 2014, along which the altitudes indicated by h1, h2 and h3 in the left panel of Figures 1 and 2. The bottom panels of Figures (9-14) indicate the wavelet analysis of the oscillations over 24 minutes and 19 minutes for two data. The hatched area is the shape of an area in which the wavelet power spectrum is disturbed due to the effect of the endpoints of finite longitudinal signals. The hatched area outside the curve is used to remove the edge effects and indicate the cone of influence region (COI) where the wavelet power spectra are distorted because of the influence of the end points of finite-length signals. These effects will not be reliable and will be eliminated.

4 Conclusion and discussion

In this study, by using spectral images obtained from the *IRIS* Telescope, one will be able to detect Doppler shift fluctuations. Accordingly, by analyzing the spectral profiles for three altitudes, the amplitude of the Doppler velocities and the dominant frequencies of the Doppler oscillations were determined. Doppler velocity in the first data for the three altitudes was obtained from -30 to 48 $km\ s^{-1}$, -36 to 12 $km\ s^{-1}$ and -18 to 21 $km\ s^{-1}$, respectively. Average Doppler velocity range in the second data for the three altitudes is obtained from -72 to 87 $km\ s^{-1}$, -84 to 93 $km\ s^{-1}$, and -84 to 78 $km\ s^{-1}$. Results of wavelet analysis of spectral fluctuations of Si IV 1402 spectra for the first data recorded on January 27, 2014, along the three altitudes (indicated by h1, h2 and h3) show that the 4 and 5, 3, and 3 and 5 minutes fluctuations are predominant. In the second data, predominant period in the three altitudes were determined as 5, 5, 1.5, and 3 minutes. Because the spicules and small jets are almost in the vertical direction, the resulting velocities due to fluctuations along the line of sight can be considered the transverse velocities of them. Photospheric convective motions are often the source of wave excitation in magnetic tubes [33]. Therefore, the propagation of waves in the chromosphere can be traced through their dynamic. The cut-off frequency in the chromosphere is 3 minutes. This means that only waves with a period of less than 3 minutes can penetrate to the higher layers. Authors in [9] claimed that the period of wave propagation increases with increasing temperature and plasma density and, the most significantly, their angle tilt, therefore waves with 5-minute periods can also propagate. Magnetic tubes conduct three types of waves: the kink modes, sausage modes, and rotating Alfvenic waves. Some of these waves can cause Doppler displacement observations. Rotating Alfven waves in thin tubes cause periodic non-thermal flattening of spectral lines but do not cause Doppler displacement fluctuations [33]. Sausage modes cause fluctuations in the intensity of the lines due to density changes, and if the axis of the tube is at an angle to the vertical line, the longitudinal velocity field of the sausage modes can cause Doppler displacement changes. But the main contribution to Doppler displacement fluctuations is due to kink modes, which fluctuate transversely perpendicular to the axis of the tube[34]. Authors in [22] determined the unsigned line of sight velocities of the spicules to be slightly less than 10 $km\ s^{-1}$. In [7] and [20] authors achieved velocities perpendicular to the main axis of the spicules between 5 and 30 $km\ s^{-1}$. For example, in [10] authors identified two types of transverse motions in spicules: (1) Swaying motions of 15 to 20 $km\ s^{-1}$ and (2) Torsional motions in the range of 24 to 20 $km\ s^{-1}$. They reported that Alfven waves with amplitudes of 10 to 25 $km\ s^{-1}$ with periods of 100 to 500 seconds and could penetrate chromosphere. By analyzing the Mg II spectrum, the speed of the spicules along the field of view was obtained as -25 to 25 $km\ s^{-1}$ so that the average asymptomatic speed of the spicules was from 2 to 10 $km\ s^{-1}$ [31]. Authors in [35] investigated solar spicule oscillations and found that the most prominent period wave are about 30-500 s as periodic transverse displacements of the spicule axis. They have been interpreted as fast kink magneto-acoustic modes (Alfvenic waves). Authors in [27] studied spicules and determined their frequencies at about 5.5 mHz (3 min). In [17] authors studied Hinode/SOT-filtergrams observations of intensity fluctuations in the Ca II H line and the G-band and analyzed the intensity oscillation spectra and found that non-magnetic intensity fluctuations show a strong oscillatory power in the 3 to 7 mHz which is consistent with our obtained values. In [30] authors studied chromospheric peculiar off-limb dynamical events based on *IRIS* observations and detected the period of the best observed fast waves of order of 100 s which could be related to the spinning motions of spicules, which is consistent with our obtained values. According to our results, it was suggested that the fluctuations in the Brueckner events with one wing enhancement and both wing enhancements, illustrated the swaying and rotational motions over their axes, respectively. Summery, we have detected the swaying and rotational motions of spicules over their axes by analyzing the Brueckner events spectra based on *IRIS* observations with average Doppler velocity of 35 to 80 $km\ s^{-1}$ and period of 1.5 to 5 minutes for two data. The swaying and rotating motions can propagate the kink and twisted Alfvenic supper and hyper sonic waves, respectively.

Acknowledgment

The authors gratefully acknowledge the use of data from the *IRIS* databases. *IRIS* is a NASA small explorer mission developed and operated by LMSAL with mission operations executed at NASA Ames Research center and major contributions to downlink communications funded by ESA and the Norwegian Space Centre.

References

[1] Antolin, P., Schmit, D., Pereira, T. M. D., De Pontieu, B., & De Moortel, I. 2018, ApJ., 856, 44A.

[2] Brueckner, G. E., & Bartoe, J. D. F. 1983, ApJ., 272, 329.

[3] Chae, J., Wang, H., Lee, C. Y., Goode, P. R., & Schühle, U. 1998, ApJ., 504, L123.

[4] Chen, Y. J., Tian, H., Huang, Z., Peter, H., & Samanta, T. 2019, ApJ., 873, 79.

[5] Curdt, W. & Tian, H. 2011, Astron. Astroph., 532, L9.

[6] Curdt, W., Tian, H., & Kamio, S. 2012, SoPh., 280, 417.

[7] De Pontieu, B., McIntosh, S. W., Carlsson, M., Hansteen, V. H., Tarbell, T. D., & et al. 2007, Science, 318, 1574.

[8] De Pontieu, B., Rouppe van der Voort, L., McIntosh, S. W., Pereira, T. M. D., Carlsson, M., & et al. 2014, Science, 346.

[9] De Pontieu B., Erdélyi, R., & James S. P. 2004, Nature, 430, 536.

[10] De Pontieu, B., Carlsson, M., Rouppe van der Voort, L. H. M., Rutten, R. J., Hansteen, V. H., & Watanabe, H. 2012, ApJ., 752, L12.

[11] De Pontieu, B., Title, A. M., Lemen, J. R., Kushner, G. D., Akin, D. J., Allard, B., & et al. 2014, SoPh., 289, 2733.

[12] Dere, K.P., Bartoe, J. D. F., & Brueckner, G. E. 1984, ApJ., 281, 870.

[13] Dere, K. P., Bartoe, J. D. F., & Brueckner, G. E. 1989, SoPh., 123, 41.

[14] Dere, K. P. 1992, Solar Wind Seven Colloquium, 11.

[15] Doyle, J. G., Popescu, M. D., & Taroyan, Y. 2006, Astron. Astroph., 446, 327.

[16] Hong, J., Ding, M. D., Li, Y., Fang, C., & Cao, W. 2014, Astrophys. J., 792, 13.

[17] Lawrence, J. K., Cadavid, A. C. 2012, Solar Phys., 280, 125.

[18] Langangen, Ø., De Pontieu, B., Carlsson, M., Hansteen, V. H., Cauzzi, G., & Reardon, K. 2008, ApJ., 679, L167.

[19] Nakariakov, V. M., & Verwichte, E. 2005, Living Rev. Solar Phys., 2, 1.

[20] Pereira, T. M. D., De Pontieu, B., & Carlsson, M. 2012, ApJ., 759, 18.

[21] Ning, Z., Innes, D., & Solanki, S. 2004, Astron. Astroph., 419, 1141.

[22] Pasachoff, J. M., Jacobson, W. A., & Sterling, A. C. 2009, SoPh., 260, 59.

[23] Pereira, T. M. D., De Pontieu, B., Carlsson, M., Hansteen, V., Tarbell, T. D., Lemen, J., & et al. 2014. ApJ., 792, L15.

[24] Roberts, B. 2004, MHD Waves in the Solar Atmosphere, ESA SP., 547.

[25] Rouppe van der Voort, L., Leenaarts, J., de Pontieu, B., Carlsson, M., & Vissers, G. 2009, ApJ., 705.

[26] Tavabi, E., Koutchmy, S., & Golub, L. 2015a, SoPh., 290.

[27] Tavabi, E., Koutchmy, S., Ajabshirizadeh, A., Ahangarzadeh Maralani, A. R., & Zeighami, S. 2015b, Astron. Astroph., 573, 7.

[28] Tavabi, E., Ajabshirizadeh, A., Ahangarzadeh Maralani, A. R., & Zeighami, S. 2015c, JApA., 36, 307T.

[29] Tavabi, E. 2018, MNRAS., 476, 868.

[30] Tavabi, E., & Koutchmy, S. 2019, ApJ., 883, 41T.

[31] Tei, A., Gun, S., Heinzel, P., Okamoto, T., Stepan, J., Jejcic, S., & Shibata, K. 2020, ApJ., 888, 2T.

[32] Torrence, C., & Compo, G. P. 1998, BAAS., 79, 61.

[33] Zaqarashvili, T. V. 2003, Astron. Astroph., 399L.

[34] Zaqarashvili, T. V., Khutsishvili, E., Kukhianidze, V., & Ramishvili, G. 2007b, Astron. Astroph., 474, 627.

[35] Zaqarashvili, T. V., Erdlyi, R. 2009, Space Sci. Rev., 149, 355.

[36] Zeighami, S., Ahangarzadeh Maralani, A. R., Tavabi, E., & Ajabshirizadeh, A. 2016, SoPh., 291, 847.

[37] Zeighami, S., Tavabi, E., & Amirkhanlou, E., 2020, JApA., 41, 18Z.

[38] Zhang, M., Xia, L. D., Tian, H., & Chen, Y. 2010, Astron. Astroph., 520, A37.